The effect of contact severity on micropitting: simulation and experiments

Ye Zhou[1,2], *Caichao Zhu*[1*], *Benjamin Gould*[2]

Nicholaos G. Demas[2], *Huaiju Liu*[1], *Aaron C. Greco*[2]

[1]*State Key Laboratory of Mechanical Transmissions, Chongqing University, Chongqing 400030, China*

[2]*Applied Materials Division, Argonne National Laboratory, Argonne IL 60439, USA*

* *Corresponding author：cczhu@cqu.edu.cn*

Abstract: A numerical contact fatigue model combining the effects of rolling contact fatigue and wear has been developed based on mixed elastohydrodynamic lubrication (EHL) theory, continuum damage mechanics (CDM) and the Archard's wear law. A series of benchtop tests were conducted using a triple-contact test rig to study the influence of surface roughness, speed and load on micropitting. The proposed surface damage model was used to simulate the rolling-sliding line contact of surfaces having different surface topography. The film thickness, contact pressure and sub-surface stress were determined by solving the generalized Reynolds equation and using the well-developed discrete convolute and fast Fourier transformation (DC-FFT) method. The jump-in-cycle was assumed to evaluate the accumulated damage based on the tested fatigue life and sub-surface stress histories. Surface topography was updated by calculating the wear height with the Archard's wear equation. Results reveal that micropitting occurs under the combined effect of wear and contact fatigue. The micropitting rate increased then turn to decreased as the lambda ratio (λ) increased. The contact pressure significantly affected the contact fatigue life and the micropitting rate.

Keywords: Micropitting; Mixed elastohydrodynamic lubrication; Contact fatigue; Film thickness ratio.

Nomenclature

b	Half Hertzian contact width (m)
C_{ij}^{p}, C_{ij}^{q}	Force-stress influence coefficient $(-)$
D	Total accumulated damage $(-)$

E_1, E_2	Elastic modulus of roller and ring (Pa)
E_0	Effective elastic modulus (Pa)
h	Film thickness (m)
h_0	Gap height between surfaces (m)
h_g	Geometry gap between surfaces (m)
H_a	Material hardness (Pa)
k_{dry}, k_{lub}	Wear coefficient of dry contact and lubrication regime, respectively (−)
m, τ_r	Material dependent parameters related with damage (Pa)
N	Fatigue life cycle (−)
p	Surface pressure (Pa)
p_H	Hertzian maximum pressure (Pa)
q	Shear traction (Pa)
$\boldsymbol{S}_{ij}$	The deviatoric stress tensor (Pa)
Sa	Arithmetical mean height of the surface (m)
Sq	Root mean square height of the surface (m)
S_u	Surface roughness height (m)
t	Time (s)
u_s	Sliding velocity (m/s)
u_r	Rolling velocity (m/s)
v_1, v_2	Poisson's ratio of roller and ring (−)
V_e	Elastic deformation (m)
W_n	Applied load (N)
x, y, z	Coordinates (x is parallel to rolling direction) (−)
α	Pressure–viscosity coefficient (−)
η	Viscosity of the lubricant (Pa · s)
η_0	Ambient viscosity of the lubricant (Pa · s)
η^*	Equivalent viscosity of the Eyring fluid (Pa · s)
ρ	Current density of the fluid (kg/m^3)
ρ_0	Ambient density of the lubricant (kg/m^3)

ΔN	The number of cycle interval $(-)$
ΔD	The increment of the damage variable $(-)$
Δh_w	Wear depth (m)
$\Delta \tau_{oct}$	Octahedral shear stress (Pa)
λ	Film thickness ratio $(-)$
μ	Average coefficient of friction $(-)$
τ	Film shear stress (Pa)
τ_0	Eyring characteristic shear stress (Pa)
$IFFT$	Inverse Fourier transform$(-)$

1.Introduction

Micropitting is a typical surface fatigue failure mode associated with rolling-sliding contacts in bearings and gears. If left unchecked, micropitting can lead to decreasing of reliability, and premature failure in numerous applications such as wind turbines, helicopters and automobiles, etc. [1, 2]. It is generally accepted that micropitting is sensitive to the severe stress concentrations at or very near the contacting surfaces [3, 4]. It follows that the lubrication condition of the contact, as determined by the operating conditions, lubricant properties and surface topography, has a drastic effect on both the presence, as well as the rate, of micropitting. Instances where the contact roughness and lubricant film thickness have similar magnitudes, often mentioned as mixed lubrication, are known to promote the formation of micropits [5]. The contact severity represented by the lambda value (λ), i.e. the ratio of film thickness to composite surface roughness, strongly influences micropitting [6].

Recent development of mixed EHL studies and experimental designs provide effective ways for a better understanding of micropitting mechanism. Zhu et al. [7] proposed a micropitting life prediction approach based on a mixed EHL model, calculated contact fatigue life by using the Zaretsky's life prediction equation with the von Mises stress field and compared the influence of surface finish on fatigue life. Evans et al. [8, 9] performed a micro-EHL simulation of two surfaces in contact and analyzed the contact fatigue and damage accumulation. These works showed the predicted damage is concentrated close to surfaces and verified that in many practical gear designs, it is possible to improve micropitting performance by specifying a lower RMS

value. Li and Kahraman [3, 10] developed a micropitting model based on mixed EHL and mutil-axial fatigue criteria to predict the crack initiation life. They defined the micropitting severity index (MSI) as the cumulative probability of fatigue failure to quantify micropitting failure. Webster and Norbart [11] investigated various operating parameters and found that the micropitting rate increased with the decreasing specific film thickness, increasing load and negative relative sliding. Oila and Bull [12] adopted a fractional factorial design with a twin disk machine to assess the influence of different lubricant, load, temperature, etc. It was suggested that micropitting is related to the martensite decay. Very recently Zhang et al. [13] and Wang et al. [14] studied the contact fatigue damage evolution with a ratchetting-multiaxial fatigue damage approach and a crystal-plasticity based approach, respectively. Through a twin-disc tribometer, Rabaso [15] et al. found that an increasing SRR tends to reduce the material's resistance to RCF, until a threshold SRR is reached when wear becomes predominant. In engineering practice, micropitting decreases in severity as contact slip decreases, but it is also found in the pure rolling condition [16].

Using a triple-contact disc tester and a reciprocating sliding rig, Laine et al. [17] observed a nearly inverse interrelation between the mild wear in the sliding test and the micropitting in the three-ring-on-roller test. Morales-Espejel and Brizmer [18] developed a model enable to capture the competitive mechanism between surface contact fatigue and mild wear, which showed a qualitative agreement between simulations and tests. By simulating surface rolling contact fatigue and comparing the predicted and measured surface roughness, Brandao et al. [19] suggested the need to combine wear and surface contact fatigue damage for successful modeling of micropitting. Recently, Morales-Espejel et al. [20] investigated micropitting on the surface of spur gears by using the model mentioned above and several disc-roller tests. The result showed that the severity of micropitting is strongly depended on the interaction between surface fatigue and mild wear. However, most of the tests just run for few million cycles to obtain micropitting, which failed to reflect the surface damage behavior of the entire service term in high-cycle contact fatigue.

In this paper, the influence of film thickness ratio, sliding and load on micropitting behavior was evaluated numerically and experimentally. A series of rolling-sliding contact fatigue tests were performed with a three-ring-on-roller micropitting rig allowing to change or isolate contact parameters and maintain long-term tests. The surface damage prediction model was developed

by combining mixed elastohydrodynamic lubrication (EHL), continuum damage mechanics (CDM) and the Archard's wear law. The effects of contact pressure, surface roughness and velocity on rolling-sliding contact performance were investigated. The micropitting damage was evaluated by combining the tested contact fatigue life and the theoretical damage accumulation approach.

2. Modeling Methodology

The model developed in the present work consists of three major parts, as illustrated in Fig. 1. The first part of the model utilizes a mixed EHL approach, considering the transient effect during the determination of the surface pressure and film thickness. The sub-surface stress field is calculated at every instant, then the stress history is obtained at each critical material point. Secondly, the stress history is combined with the CDM to evaluate surface damage. Subsequently the surface topography is updated using the wear equation.

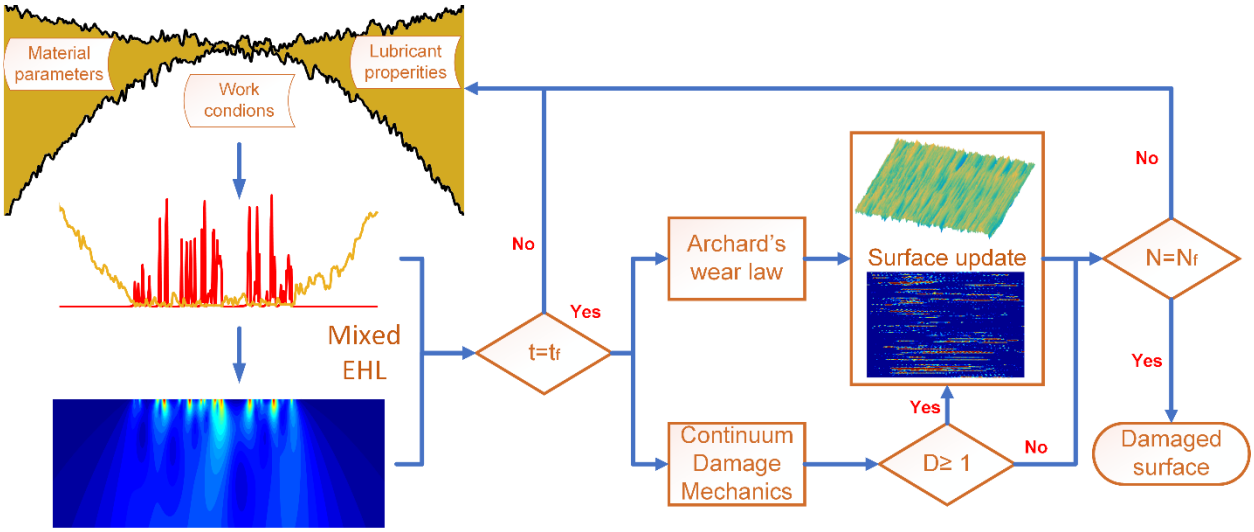

Fig. 1 Schematic diagram of the surface damage model

2.1. EHL equations and sub-surface stress

The basic EHL model is governed by the generalized Reynolds equation [21]

$$\frac{\partial}{\partial x}\left(\frac{\rho h^3}{12\eta^*}\frac{\partial p}{\partial x}\right)+\frac{\partial}{\partial y}\left(\frac{\rho h^3}{12\eta^*}\frac{\partial p}{\partial y}\right)=\frac{\partial(\rho u h)}{\partial x}+\frac{\partial(\rho h)}{\partial t} \tag{1}$$

The film thickness at every instant is given as

$$h=h_0(t)+h_g+V_e(x,y,t)-S_u(x,y,t) \tag{2}$$

where $h_0(t)$is the initial separation between two contact surfaces determined by the load balance condition; h_g is the surface gap; S_u denotes composite roughness height of two surfaces; V_e represents the total elastic deformation calculated by using the Boussinesq's equation and the DC-FFT algorithm [22]

$$\mathrm{V}_e(x,y) = \frac{2}{\pi E_0}\iint \frac{p(x,y)}{\sqrt{(x-\xi)^2+(y-\eta)^2}}\mathrm{d}\xi\mathrm{d}\eta \tag{3}$$

A cut-off value of 5 nm is assumed for the minimum film thickness to guarantee the continuity of lubricant [23]. According to Zhu et al. [24, 25], in the area where the film thickness lowers than the limit, it is assumed the asperities contacts take place and the pressure flow disappears, then the Reynolds equation is reduced as

$$\frac{\partial(uh)}{\partial x} + \frac{\partial h}{\partial t} = 0 \tag{4}$$

The pressure controlled by the Reynolds equation should satisfy the load equilibrium over the entire solution domain.

$$\iint p(x,y)\,\mathrm{d}x\mathrm{d}y = W_n \tag{5}$$

The pressure related lubricant density is described by the Dowson-Higginson equation [26]

$$\rho = \rho_0 \frac{0.59\times10^9+1.34p}{0.59\times10^9+p} \tag{6}$$

The Ree-Eyring fluid is used to represent the non-Newtonian behavior with the effective viscosity

$$\eta^* = \eta\left(\frac{\tau}{\tau_0}\right)/\sinh\left(\frac{\tau}{\tau_0}\right) \tag{7}$$

where τ_0 is the characteristic stress given as $\tau_0 = 5$ MPa. The viscosity η can be described as a function of the pressure [27]

$$\eta = \eta_0 \exp\{(\ln\eta_0 + 9.67)[(1+5.1\times10^{-9}p)^{z_e}-1]\} \tag{8}$$

where z_e is calculated by pressure–viscosity coefficient α, $z_e = \alpha/[5.1\times10^{-9}(\ln\eta_0+9.67)]$. The shear traction on the surface can be determined as [28]

$$q = \frac{\tau_0 \ln\left(\sqrt{{u_s}^2-\left(K_1^2-K_2^2\right)^2}-u_s\right)}{K_1+K_2} \tag{9}$$

where $K_1 = \int_0^h \frac{\tau_0}{\eta}\cosh\left(\frac{z_1}{\tau_0}\frac{\partial p}{\partial x}\right)\mathrm{d}z_1$, $K_2 = \int_0^h \frac{\tau_0}{\eta}\sinh\left(\frac{z_1}{\tau_0}\frac{\partial p}{\partial x}\right)\mathrm{d}z_1$.

Once the surface pressure and shear traction are obtained, the instantaneous sub-surface stress field can be calculated efficiently through the DC-FFT algorithm with predetermined influence coefficient [29]

$$\sigma_{ij} = \mathrm{IFFT}(C_{ij}^{p}(x-k, y-l)\tilde{p}(k,l) + C_{ij}^{q}(x-k, y-l)\tilde{q}(k,l)) \quad (10)$$

where IFFT is inverse fast Fourier transform, $\tilde{p}$ and $\tilde{q}$ are surface traction in frequency domain. C_{ij}^{p} and C_{ij}^{q} are force-stress influence coefficient of which explicit expression can be found in Ref. [29].

2.2. Damage accumulation prediction

The occurrence of micropitting is related to the fatigue damage accumulation, which continuously increases within the stress-concentration region until a critical level is reached [30]. The continuous damage mechanics (CDM) provides a potential way to evaluate micropitting. The cracks of micropitting have a very short propagation duration, which means the total life of a crack is almost equal to the crack initiation time [31]. It can be considered that the accumulated damage with the critical value indicates the generation of a micropit [18]. In the present study, the damage variable D is introduced to evaluate the micropitting based on CDM. For multiaxial cyclic loading, when the perfectly elasticity assumed, the evolution of the damage variable D can be given as

$$\frac{\mathrm{d}D}{\mathrm{d}N} = \left[\frac{\Delta\tau_{oct}}{\tau_r(1-D)}\right]^m \quad (11)$$

where N denotes the contact cycle number, τ_r and m are material constants, which can be obtained based on the uniaxial torsional S-N curve. For the material used in the current study, AISI 52100 steel, the parameters are given by [32]

$$m = 10.1, \tau_r = 6113 \text{ MPa}$$

According to the failure-causing stress [33], the critical stress is selected as the octahedral shear stress amplitude, $\Delta\tau_{oct}$, which is given by the deviatoric stress tensor $\boldsymbol{S}_{ij}$

$$\Delta\tau_{oct} = \max\left[\left(\frac{1}{3}\boldsymbol{S}_{ij}\boldsymbol{S}_{ij}\right)^{1/2}\right] \quad (12)$$

For a high-cycle contact fatigue, it is computationally infeasible to simulate every loading cycle. An accelerated approach named the jump-in-cycle developed by Lemaitre [34] can be used to evaluate the high-cycle fatigue damage. In the approach the state of stress and the damage increment are assumed constant over a limit number of cycles, ΔN, in each element. The deterioration of material properties caused by the fatigue damage is neglected according to previous continuous damage based studies [14, 30]. Within the given finite cycle the damage increment was determined as

$$D = \sum_{i=1}^{n} \left(\frac{dD}{dN}\right)_i \Delta N \tag{13}$$

In this study, the total contact cycle is determined by triple-contact fatigue tests, and divided into many blocks by the cycle interval ΔN. The damage accumulates in each contact block and micropits are generated at locations where damage reaches the critical value. After the fatigue life reached, the total damage estimation is reported in terms of micropitted surface area.

2.3. Wear model

Mild wear is a steady-state process constituted by relatively low wear rate in long contact cycles [35]. According to the Archard's wear law [36], the wear volume loss in the contact can be written as

$$\Delta V = k\frac{F_n S_t}{H_a} \tag{14}$$

where F_n is total load, S_t *is* sliding distance in a certain time and H_a is the material hardness. When the micro-contact between asperities is considered in the mixed-EHL, the local wear state should be related with the lubrication condition and the wear law can be given as

$$\frac{\Delta h_w}{\Delta t} = \frac{k(x,y)p(x,y,t)u_s(x,y)}{H_a} \tag{15}$$

where Δh_w is the height removed from the material; p is the local pressure and u_s is the sliding speed. k is the local wear coefficient which should not be treated as a constant since there might be dry contact between asperities in the contact zone. In present study, $k_{dry} = 1 \times 10^{-11}$ and a ratio of $k_{dry}/k_{lub} = 5$ were assumed based on former studies [18, 20], where k_{dry} and k_{lub} denote the wear coefficient of asperity contact and lubrication regime, respectively.

3. Comparison to roller-discs tests

3.1. Experimental procedure

The tests were performed using a micropitting rig developed by PCS Instruments, as shown in Fig. 2. The central roller and three discs (rings) are driven by two motors separately, which allows a large range of slide-to-roll ratio (SRR). Load is applied by a stepper motor on the top ring, providing a load range of $0 - 2000$ N. A thermocouple and a customized cooler system maintain a specified oil temperature. The failure criterion is set based on the real-time measured coefficient of friction, vibration acceleration and temperature.

The material of the rings and rollers was AISI 52100 steel with surface hardness of 60 and 63 HRC (for wear equation the hardness is assumed as $H_a \approx 7$ GPa), respectively. The diameters of the rings and roller were 54 mm and 12 mm, respectively. The width of contact trace on the roller was 1 mm. The roller and rings were splash-lubricated with a fully formulated, ISO viscosity grade 68, semi-synthetic gear oil. The lubricant parameters are shown in Table 1. All the tests were performed at an ambient temperature of 100 ℃. The surface finish of the specimens was ground which provides the consistent surface topography of rollers and rings. All samples were pre-examined and the surface roughness and width of the track were measured before every test. The white light interferometer (ContourGT-K, Bruker, Tucson, AZ·USA) was used to measure surface roughness. The parameters of surface topography was calculated based on ISO 25178 standard [37]. Fig. 3 shows surface topographies of a roller and two rings, with Sa (arithmetical mean height of the surface) roughness of 0.2 μm, 0.25 μm and 0.42 μm, respectively.

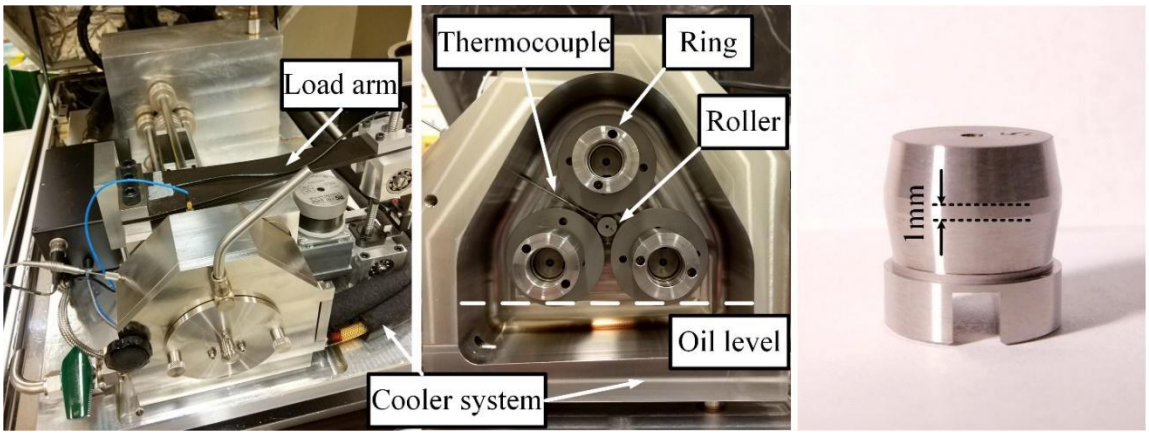

Fig.2 PCS Instruments triple-contact micropitting rig (MPR) and the test roller with a 1-mm-wide wear track

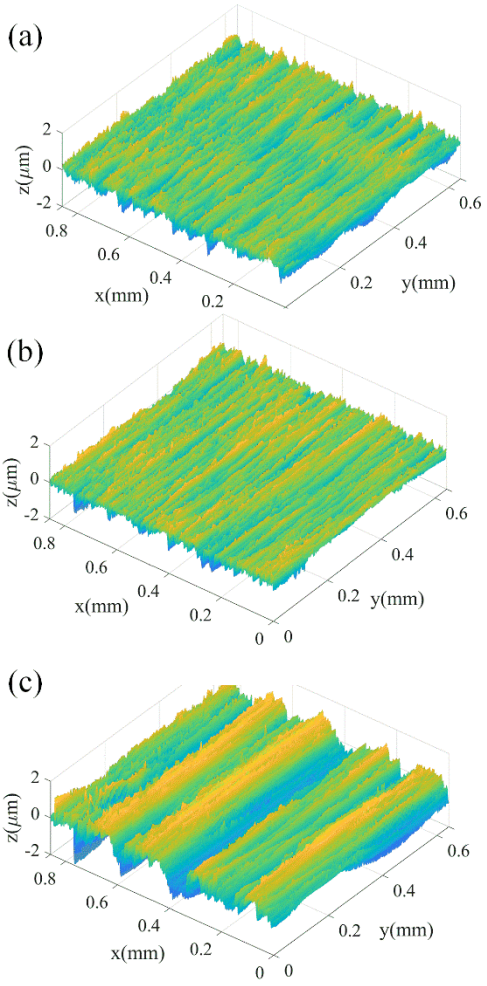

Fig.3 Surface topography of (a) roller, $Sa = 0.2\mu m$,
(b) ring1, $Sa = 0.25\mu m$, (c) ring2, $Sa = 0.42\mu m$

Seven tests were conducted to evaluate the effect of lambda ratio, speed and load on the micropitting performance, as shown in Table 2. These tests were previously reported in Refs. [38, 39]. The lambda ratio is defined as the lubricant film thickness divided by the composite root mean square roughness, where the reference film thickness was calculated empirically by the Hamrock-Dowson equation for smooth line contacts [40]. To study the effect of λ value, the rings with surface roughness of $0.2 - 0.5$ μm were chosen, while the roughness of rollers was kept at the same level of $0.2 - 0.25$ μm. The slide-to-roll ratio, calculated by Eq. (16), was selected as -30% for all the tests.

$$SRR = \frac{2(u_{ring} - u_{roller})}{u_{ring} + u_{roller}} \tag{16}$$

The first four tests altered the λ ratio, by varying component speed and surface roughness while maintaining a constant operating stress of 1.9 GPa. The other three tests were conducted at different load levels to study the effect of contact pressure on the micropitting. The surface was inspected around the roller after it failed or reached the contact cycle limit of 100 million. This inspection was performed every 90 degrees at four predefined circumferential angles and the surface damage was recorded. The micropitting rate is defined as the ratio of micropitted area to the inspected surface area. The sample was sectioned circumferentially after the surface examination.

3.2. Numerical simulation

The experiments are simulated using the numerical model presented above. The solution domain is $-2 \le x/b \le 2$, $-2 \le y/b \le 2$ which is discretized to a grid of 257×257. In z direction, a 20-layers grid is used to simulate the depth of $0.2b$. The maximum local pressure is limited to 8 GPa. The convergence criteria of the EHL solution at any transient moment is chosen as $\sum\sum|p - p'| / \sum\sum|p| \le 1.0 \times 10^{-5}$ and $|W_n - W_n'|/W_n \le 1.0 \times 10^{-4}$. In each contact block, the EHL approach is performed in 16 time steps to obtain the pressure, film thickness and stress history at the entire domain. The ambient viscosity is $\eta_0 = 0.016$ Pa · s and corresponding pressure–viscosity coefficient is $\alpha = 15$ GPa^{-1} at 100 ℃.

The contact fatigue life obtained from tests are used to simulate the contact cycles N, which might up to one hundred million cycles. To balance the calculation accuracy and efficiency, a cycle interval of $\Delta N = 1 \times 10^6$ is adopted in the jump-in-cycle procedure. Based on the stress histories, the accumulated damage is evaluated with CDM and micropits are generated when the damage reaches the critical value. In addition, the wear height is calculated with the Archard's law and the surface roughness is updated. The procedure is repeated until the final experimental failure life is anticipated.

Tab. 1 Parameters of the lubricant and the material

Oil density (kg/m^3)	847
Kinematic viscosity at 40 ℃ (cSt)	146
Kinematic viscosity at 100 ℃ (cSt)	19
Dynamic viscosity at 100 ℃(Pa · s)	0.016

Viscosity-pressure coefficient	1.5×10^{-8}
Young's modulus (GPa)	210
Poisson's ratio	0.3
Operating temperature T_0	100 ℃

Tab. 2 Parameters of tests

Test #	Contact Stress (GPa)	Rolling Speed (m/s)	Composite Roughness Sq (nm)	μ	λ	Contact Cycles (10^6)
1	1.9	1	587	0.086	0.06	38
2	1.9	1	338	0.091	0.11	38
3	1.9	3.4	526	0.081	0.16	42
4	1.9	3.4	357	0.076	0.23	48
5	2.5	3.4	541	0.072	0.16	12
6	1.5	3.4	508	0.089	0.17	88
7	1.0	3.4	523	0.119	0.18	100

4. Results and discussion

Typical results of mixed EHL are compared with the case of smooth surface, as shown in Fig. 4. To illustrate the distribution of equivalent stress in the smooth contact, the depth in the z-direction is shown as $0 \leq z \leq b$. The pressure distribution of a smooth surface is close to the Hertzian pressure, except for the pressure spike at the outlet zone. Drastic variations in pressure and film thickness with many localized peaks and valleys can be observed. In addition, the film thickness is close to zero in areas where pressure spikes were documented, thereby denoting asperity interaction. The near surface stress field exhibits severe zones of concentration corresponding the locations of the aforementioned pressure spikes. These locations are closely related to shallow surface cracks. Fig. 5 shows micrographs of rollers after sectioning and polishing. It displays typical characteristics of micropitting close to the surface with the depths range $2.5 - 25$ μm and angles between 15 and 30 degrees [41, 42].

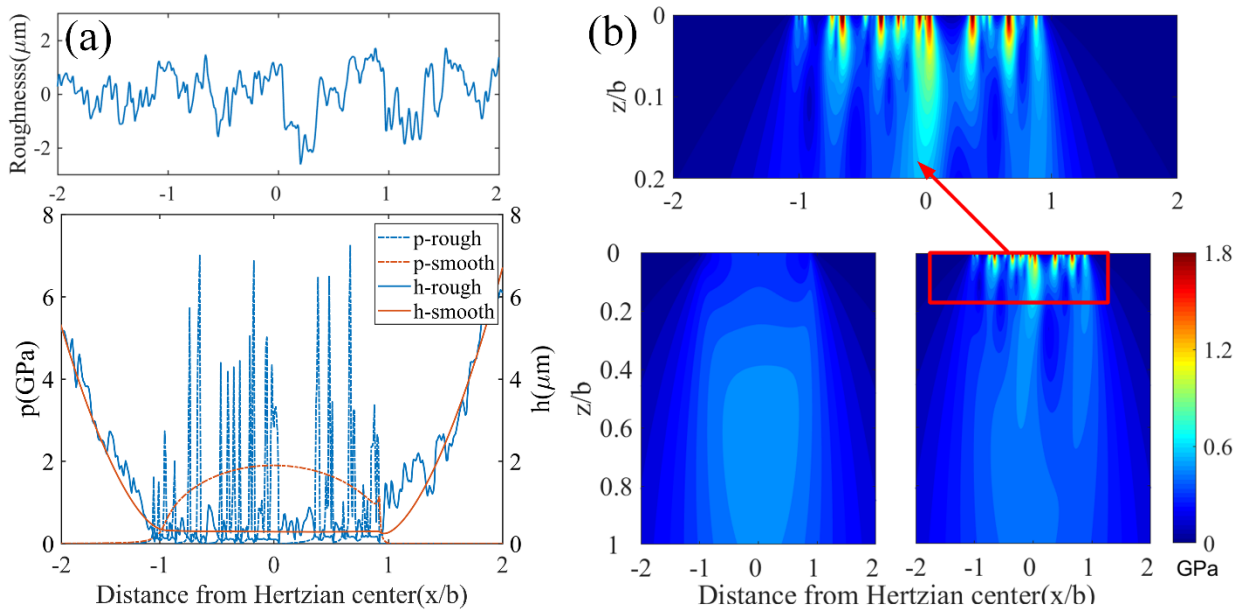

Fig. 4 The comparison between rough and smooth surface (a) distributions of roughness, pressure and thickness, (b) distributions of octahedral shear stress, $p_H = 1.9$ GPa, $u_r = 1$ m/s

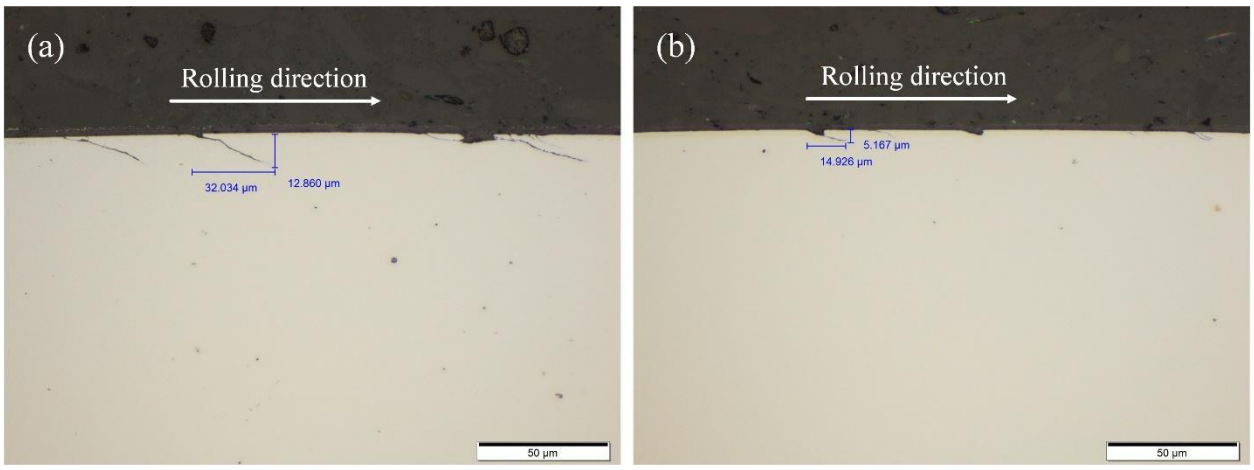

Fig. 5 Roller sub-surface after sectioning and polishing

4.1. The effect of film thickness ratio

The use of various contact conditions, as well as samples varying in surface roughness, allowed for a study of the effect of contact severity, measured through slight variations in the lambda ratio. Figs. 6-7 show the images of damaged surfaces and the plots of predicted micropitting surface, respectively. As shown in Fig. 6, the micropitting spreads along the rolling direction and distributes on the entire surface randomly. Some of the micropits show the typical

'fan' shape that have been observed in other studies [43]. In Fig. 6d, a damaged zone which resulted by the merge of several micropits could be observed, which would lead to the characteristic matte gray appearance on the surface [11]. Figs. 6a-b are the low-speed tests of $u_r = 1\ \mathrm{m/s}$ in which the intensive micropitting has not been observed. The test with the lowest λ ($\lambda = 0.06$) shows a relative smooth surface which has several transverse surface cracks. For the higher λ case ($\lambda = 0.11$) in which the surface roughness is lower, more micropitting is observed on the surface. Figs. 6c-d show the damage area caused by micropitting commonly observed at a high speed ($u_r = 3.4\ \mathrm{m/s}$). For the rougher surface with $\lambda = 0.16$, most of the surface is covered by micropitting.

Fig. 7 shows the predicted surface damage, which present banded distribution on the surface. It is postulated that the damage patch is corresponded to the high pressure region, since the pressure is significantly affected by the topography. Compared to Fig. 6, the simulation shows less micropitting than the experiment, especially in the area where the micropitting is intensive. There are two potential reasons might explain the difference between the measured and predicted results. It is postulated that the initiated micropit tends to prompt the progression of micropitting in the surrounding areas. Considering the micropit as a surface dent, it would increase the pressure and create a local high pressure ring around the dent [44]. This could aggravate the stress concentration in the surrounding area, then accelerate the progression of micropitting. Another possible reason is that three-body abrasive wear, which is also ignored in the simulation, might cause contact condition deteriorates. When the micropit occurs a small piece of material peeling off the surface might get trapped between the two surfaces which would damage the surfaces further around the initial micropitting.

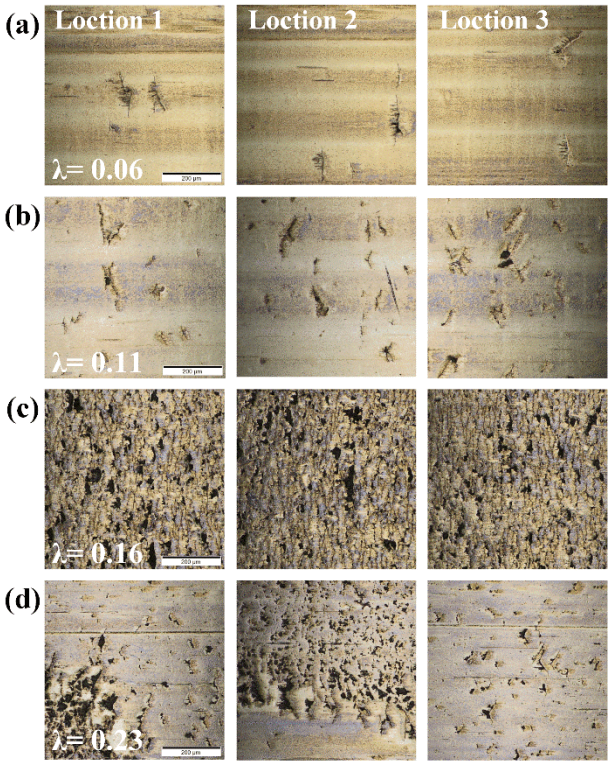

Fig. 6 The damaged roller surface of tests 1-4

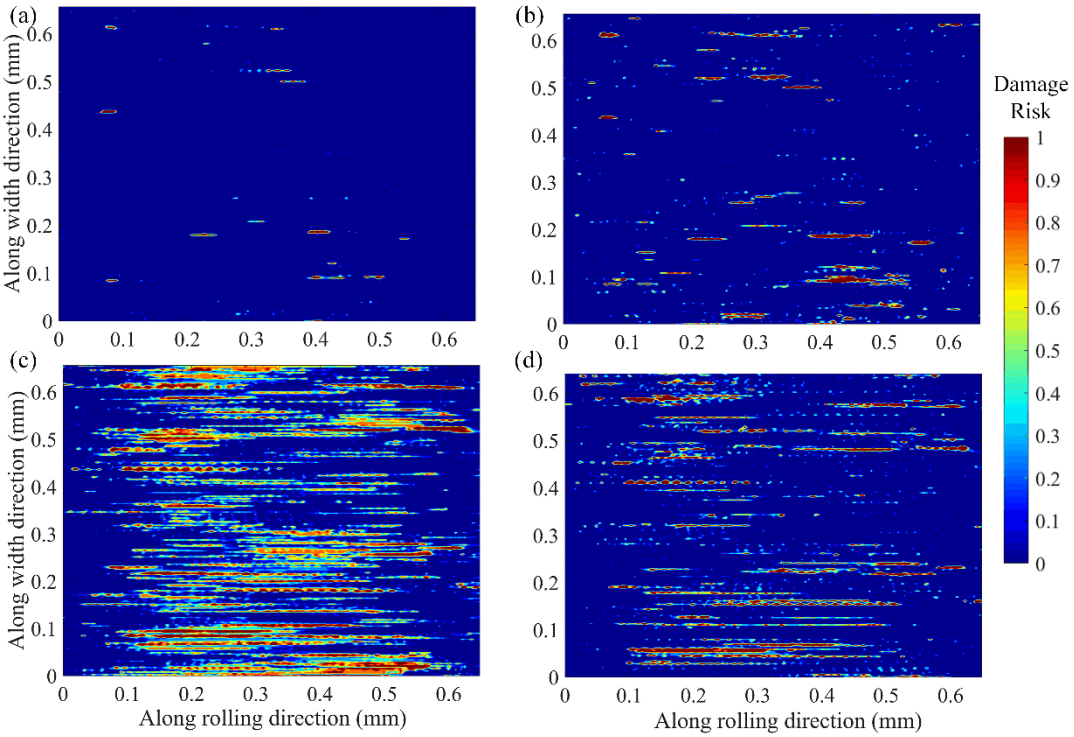

Fig. 7 Predicted damage surfaces of (a)-(d): tests 1-4

The further comparison of micropitting rate (the ratio of micropitted area to the inspected surface area) between experiment and simulation is shown in Fig. 8. The simulated values agree well with tested results. These results show that as the λ decreases, the micropitting rate does not change linearly, but rather presents a complex trend. The predicted micropitting rate, for the cases with $\lambda = 0.06$ and $\lambda = 0.11$ are 5.4% and 9.3% respectively, while for the cases with $\lambda = 0.16$ and $\lambda = 0.23$ are 31.6% and 15.7%, respectively. Comparing Test 1 and Test 3, which were identical separate from changes in rolling speed, the case of $u_r = 3.4\ \mathrm{m/s}$ (Test 3) shows a higher micropitting rate. The higher surface speed could take more asperities into contact for the same surface topography, then the corresponding material would experience more stress cycles in a unit time as the asperity passes through. However, the higher surface speed also increases the film thickness, which in turn should alleviate mild wear.

Fig. 9 shows the pressure, film thickness and sub-surface octahedral shear stress at four different λ values in the last timestep of the first loading cycle. To compare the influence of different speed and roughness on the contact performance, two different roughness of rings, $\mathrm{Sa} = 0.25, 0.42\mu\mathrm{m}$, were simulated with a same surface roughness of $\mathrm{Sa} = 0.2\ \mu\mathrm{m}$, under different rolling speed conditions. It can be noted that the pressure distribution strongly affected by the surface roughness and the pressure peaks is corresponding to the lower film thickness. The maximum octahedral shear stress can be observed at the near surface area. For the simulation results of tests 1-4, the asperity contact area ratio, which are 26.75%, 11.24%, 6.43% and 0%, respectively, decreases as λ increases. For the case with $\lambda = 0.06$ (Test 1), the higher roughness and lower rolling speed jointly promote the grid number of asperity contact. At the same speed of $1\ \mathrm{m/s}$, the ratio decreases as the roughness reduces in Test 2. For the case with $\lambda = 0.16$, the higher roughness still impacts the lubrication even the high speed would tend to increase film thickness. It is clear that the changes in the asperity contact area ratio can greatly affect the mild wear since the wear coefficient in the dry contact region is higher than that in the lubricant region.

Fig. 10 presents the evolution of sub-surface stress distribution of Test 1 from 1 million cycles to 40 million cycles. The significant change of high stress can be observed at first 20 million cycles, and the change are not very noticeable from 20 to 40 million cycles. Although the change of counter line is not remarkable, the stress concentration is greatly mitigated from 1 to 40 million cycles. It can be considered that the wear would decrease the roughness level by

removing the peaks of asperities, then reduce the pressure peaks and relieve the sub-surface stress concentration.

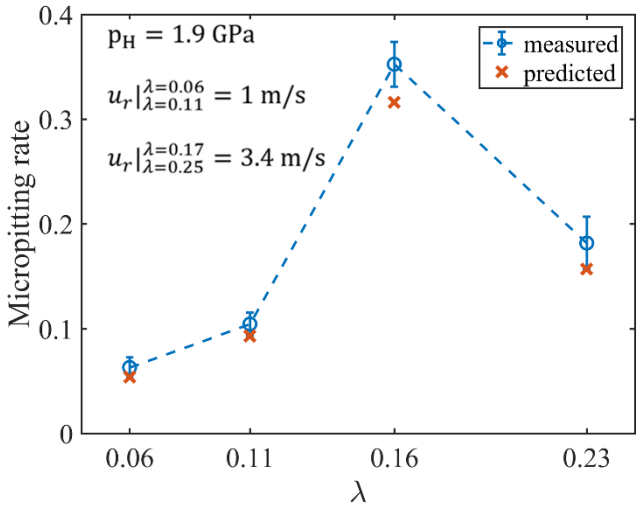

Fig. 8 Comparison between measured and predicted micropitting rate

The results presented in this section illustrate that the micropitting is not linearly dependent the λ (film thickness ratio). In this study, the maximum micropitting rate observed in the case with $\lambda = 0.16$, which has the higher speed of 3.4 m/s and ring's roughness of $Sa = 0.42$ μm. As the λ increases, the asperity contact area ratio decreases but micropitting aggravates to some extent, suggesting that wear process, which removes top of asperity, tends to suppress micropitting. Meanwhile, the initial contact state and incipient wear-in are also important for the succeeding surface damage. This is also in agreement with former research [19, 20]: the micropitting rate continuously decreases with increasing λ in the case where the surface wear is neglected, but in the case of combined fatigue and wear the micropitting rate reaches the maximum at a critical value of λ. In current study, $\lambda_{cirtical}$ should be $0.11 - 0.23$ accordingly.

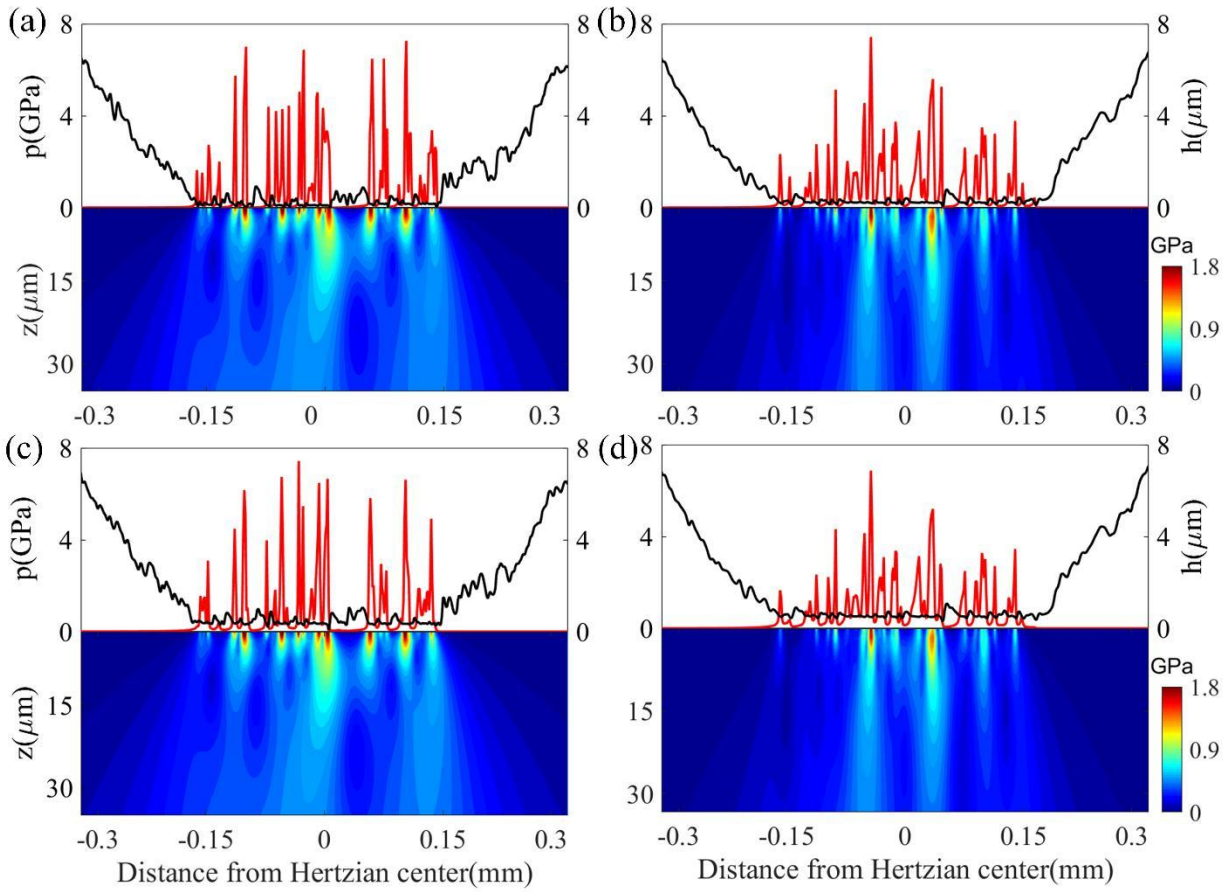

Fig. 9 The distributions of pressure, film thickness

and octahedral shear stress at $y = 0, t = t_f$ of (a)-(d): tests 1-4

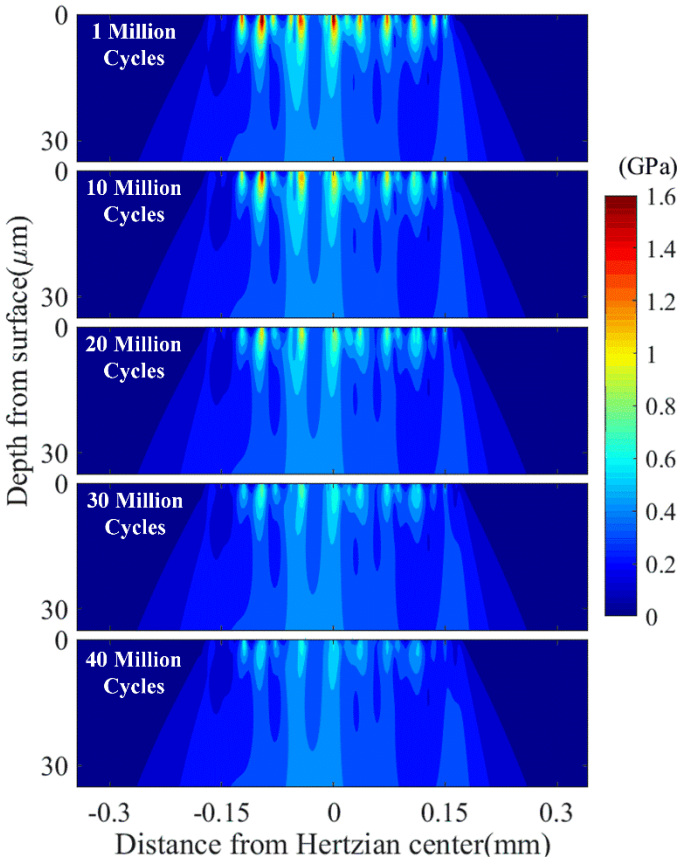

Fig. 10 The evolution of octahedral shear stress from 1 to 40 million cycles

4.2. The effect of surface pressure

The effect of load on micropitting performance was investigated in four cases of surface pressure: $1, 1.5, 1.9$ and 2.5 GPa. The lambda values of the contact remained relatively constant at $0.16 - 0.18$. The other operating conditions were same as the tests used to study the influence of λ. The images of damaged surface under different pressure conditions are shown in Fig. 11. For the case of $p_H = 1.0$ GPa, the samples did not experience failure before the run out limit of 100 million cycles. This test displayed scattered micropitting distributes on the surface under the lowest pressure, while for the case of $p_H = 1.5$ GPa, the sample failed after 88 million cycles and patches of micropitting can be observed. For heavier load cases, $p_H = 1.9$ GPa and $p_H = 2.5$ GPa, the sample failed after 42 and 12 million cycles respectively. The micropitting can be observed on the entire surface under these heavy-duty conditions. And the surface presents blue tribo-film under the highest pressure.

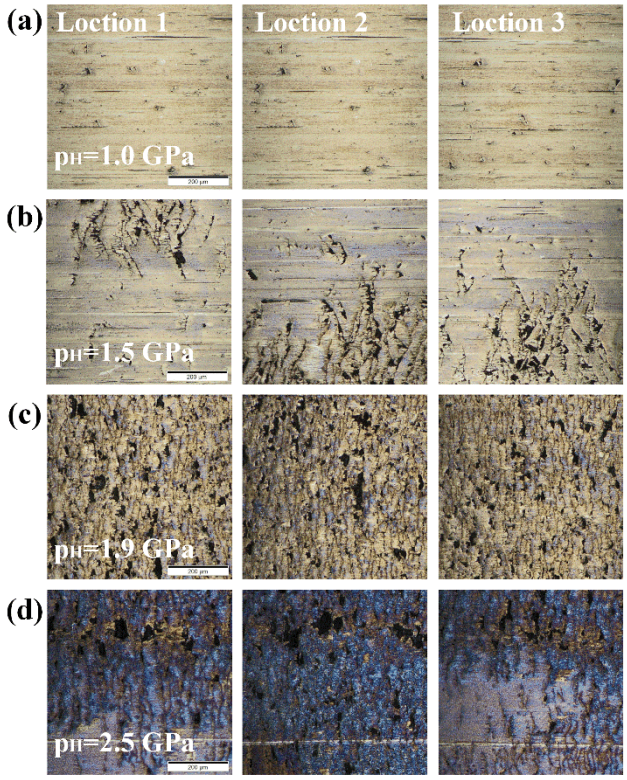

Fig. 11 Roller surface under different contact pressure (tests 3,5-7)

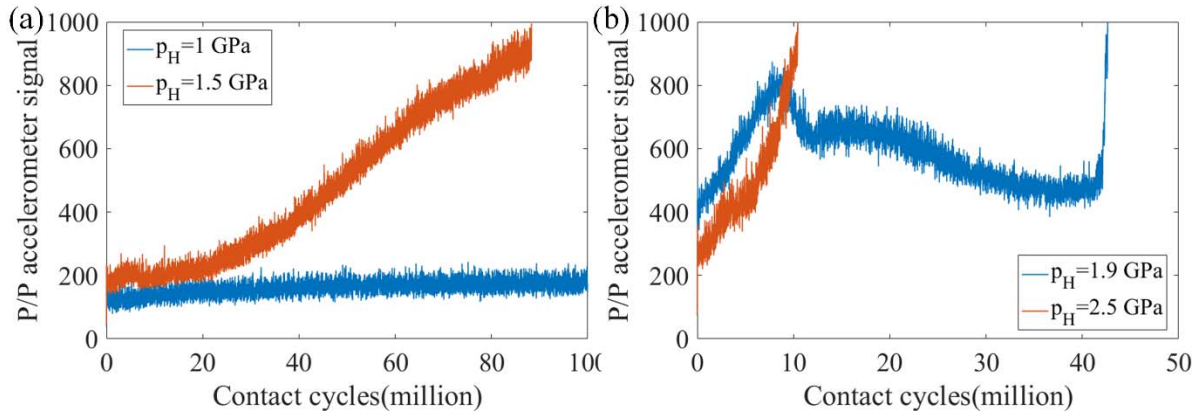

Fig. 12 The evolution of the P/P accelerometer signal of tests 3,5-7

Fig. 12 shows the evolution of the P/P accelerometer signal, measured base on the vibration of the top ring, during the entire life for the four tests. The change of vibration amplitude, to some extent, reveals the progression of micropitting and the progression rate could be roughly represented by the slope of the signal. It is clear that a higher pressure leads to a higher micropitting progression rate. For the test with $p_H = 1.9$ GPa, the rate increases firstly since the spread of micropitting, then, before reaching the limit value, a new stable state is achieved

between the damaged surface and the lubrication since the appearance of sub-surface cracks which propagates to the surface until the pit occurs. The micropitting develops continuously in the case of $p_H = 1.5$ GPa. A former research [12] showed main factors that influence the micropitting progression rate are the speed and SRR, while the contact pressure dominate the initiation of micropitting. However, in the present study, the tests under the same SRR show that the pressure also highly contributes in the progression of micropitting.

The higher pressure could exacerbate the plastic deformation, especially the regions below asperities subjected to sever plastic deformation (SPD) that might lead to microstructural changes [45]. The cracks initiated due to the accumulation of the dislocations caused by SPD and propagated along the boundary of dark etching region (DER) formed by the recrystallization at the boundary of plastic deformation region [12]. It is possible that higher pressure damages the surface before mild wear smooths it and sever micropitting induces the considerable vibration and causes failure of the samples.

5. Conclusion

In this study, a surface damage model was developed and contact fatigue tests were conducted using a triple-contact disc tester to investigate the influence of the lambda ratio and contact pressure on micropitting. The rolling-sliding contact under mixed elastohydrodynamic lubrication was simulated, the damage accumulation approach and Archard's wear law were combined to predict the surface damage. The main conclusions can be summarized as follows:

- The surface roughness and rolling speed are highly involved in surface damage. Comparing the low-speed case of $u_r = 1$ m/s and the high-speed case of $u_r = 3.4$ m/s, it is suggested that wear process significantly reduces micropitting risk. To further understand the initiation and progression of micropitting, the comprehensive modeling incorporating wear process and contact fatigue is recommended.
- Micropitting rate increases nonlinearly then decreases as the λ increases. Although reducing the surface roughness would improve the contact performance, the lubricant and work condition should be fully considered in the surface design and manufacture. In this study the critical value of the film thickness ratio should be $0.11 - 0.23$.
- Contact pressure significantly affect the contact fatigue life. For the load case of $p_H = 1.5$ GPa, the sample did not fail until 88 million cycles; but for the heavier load

case of $p_H = 2.5$ GPa, the sample failed after 12 million cycles. Higher pressure leads to the increasing of the micropitting rate.

Acknowledgements

This work is supported by the National Key R&D Program of China (Grant No. 2018YFB2001300), the National Natural Science Foundation of China (Grant Nos. 51575061, U1864210), and the Fundamental Research Funds for the Central Universities (Grant no. 2018CDXYJX0019). This work is supported by the U.S. Department of Energy Office of Energy Efficiency and Renewable Energy, Wind Energy Technology Office under Contract No. DE-AC02-06CH11357. The authors are grateful to DOE Project Managers Mr. Michael Derby and Mr. Brad Ring for their support and encouragement. Y. Z. gratefully acknowledges support from the Chinese Scholarship Council (CSC).

References

[1] Li S, Kahraman A. Micro-pitting fatigue lives of lubricated point contacts: Experiments and model validation. International Journal of Fatigue. 2013;48:9-18.
[2] Liu H, Liu H, Bocher P, Zhu C, Sun Z. Effects of case hardening properties on the contact fatigue of a wind turbine gear pair. International Journal of Mechanical Sciences. 2018;141:520-7.
[3] Li S, Kahraman A. A micro-pitting model for spur gear contacts. International Journal of Fatigue. 2014;59:224-33.
[4] Evans HP, Clarke A, Snidle R. Understanding micropitting in gears. Proceedings of the Institution of Mechanical Engineers, Part C: Journal of Mechanical Engineering Science. 2015.
[5] Wang QJ, Chung Y-W. Encyclopedia of tribology: Springer; 2013.
[6] Ahlroos T, Ronkainen H, Helle A, Parikka R, Virta J, Varjus S. Twin disc micropitting tests. Tribology International. 2009;42:1460-6.
[7] Zhu D, Ren N, Wang QJ. Pitting Life Prediction Based on a 3D Line Contact Mixed EHL Analysis and Subsurface von Mises Stress Calculation. Journal of Tribology. 2009;131:041501.
[8] Evans HP, Snidle RW, Sharif K, Shaw B, Zhang J. Analysis of micro-elastohydrodynamic lubrication and prediction of surface fatigue damage in micropitting tests on helical gears. Journal of Tribology. 2013;135:011501.
[9] Sharif KJ, Evans HP, Snidle RW. Modelling of elastohydrodynamic lubrication and fatigue of rough surfaces: The effect of lambda ratio. Proceedings of the Institution of Mechanical Engineers, Part J: Journal of Engineering Tribology. 2012;226:1039-50.
[10] Li S, Kahraman A. A fatigue model for contacts under mixed elastohydrodynamic lubrication condition. International Journal of Fatigue. 2011;33:427-36.
[11] Webster MN, Norbart CJJ. An Experimental Investigation of Micropitting Using a Roller Disk Machine. Tribology Transactions. 1995;38:883-93.
[12] Oila A, Bull SJ. Assessment of the factors influencing micropitting in rolling/sliding contacts. Wear. 2005;258:1510-24.

[13] Zhang B, Liu H, Bai H, Zhu C, Wu W. Ratchetting–multiaxial fatigue damage analysis in gear rolling contact considering tooth surface roughness. Wear. 2019.
[14] Wang W, Liu H, Zhu C, Wei P, Wu W. Micromechanical analysis of gear fatigue-ratcheting damage considering the phase state and inclusion. Tribology International. 2019.
[15] Rabaso P, Gauthier T, Diaby M, Ville F. Rolling Contact Fatigue: Experimental Study of the Influence of Sliding, Load, and Material Properties on the Resistance to Micropitting of Steel Discs. Tribology Transactions. 2013;56:203-14.
[16] Sheng S. Wind turbine micropitting workshop: a recap. National Renewable Energy Laboratory (NREL), Golden, CO.; 2010.
[17] Lainé E, Olver AV, Beveridge TA. Effect of lubricants on micropitting and wear. Tribology International. 2008;41:1049-55.
[18] Morales-Espejel GE, Brizmer V. Micropitting modelling in rolling–sliding contacts: application to rolling bearings. Tribology Transactions. 2011;54:625-43.
[19] Brandão JA, Martins R, Seabra JHO, Castro MJD. An approach to the simulation of concurrent gear micropitting and mild wear. Wear. 2015;324-325:64-73.
[20] Morales-Espejel GE, Rycerz P, Kadiric A. Prediction of micropitting damage in gear teeth contacts considering the concurrent effects of surface fatigue and mild wear. Wear. 2018;398-399:99-115.
[21] Yang P, Wen S. A Generalized Reynolds Equation for Non-Newtonian Thermal Elastohydrodynamic Lubrication. Journal of Tribology. 1990;112:631-6.
[22] Liu S, Wang Q, Liu G. A versatile method of discrete convolution and FFT (DC-FFT) for contact analyses. Wear. 2000;243:101-11.
[23] Gu Z, Zhu C, Liu H, Du X. A comparative study of tribological performance of helical gear pair with various types of tooth surface finishing. Industrial Lubrication and Tribology. 2018.
[24] Hu Y-Z, Zhu D. A full numerical solution to the mixed lubrication in point contacts. Journal of Tribology. 2000;122:1-9.
[25] Zhu D. On some aspects of numerical solutions of thin-film and mixed elastohydrodynamic lubrication. Proceedings of the Institution of Mechanical Engineers, Part J: Journal of Engineering Tribology. 2007;221:561-79.
[26] Dowson D, Higginson GR. Elasto-hydrodynamic lubrication: the fundamentals of roller and gear lubrication: Pergamon Press; 1966.
[27] Roelands C, Vlugter J, Waterman H. The viscosity-temperature-pressure relationship of lubricating oils and its correlation with chemical constitution. Journal of Basic Engineering. 1963;85:601-7.
[28] Zhou Y, Zhu C, Liu H, Song C, Li Z. A numerical study on the contact fatigue life of a coated gear pair under EHL. Industrial Lubrication and Tribology. 2018;70:23-32.
[29] Liu S, Wang Q. Studying Contact Stress Fields Caused by Surface Tractions With a Discrete Convolution and Fast Fourier Transform Algorithm. Journal of Tribology. 2002;124:36.
[30] He H, Liu H, Zhu C, Wei P, Sun Z. Study of rolling contact fatigue behavior of a wind turbine gear based on damage-coupled elastic-plastic model. International Journal of Mechanical Sciences. 2018;141:512-9.
[31] Brandão JA, Seabra JHO, Castro J. Surface initiated tooth flank damage. Wear. 2010;268:1-12.
[32] Warhadpande A, Sadeghi F, Kotzalas MN, Doll G. Effects of plasticity on subsurface initiated spalling in rolling contact fatigue. International Journal of Fatigue. 2012;36:80-95.
[33] Li F, Hu W, Meng Q, Zhan Z, Shen F. A new damage-mechanics-based model for rolling contact fatigue analysis of cylindrical roller bearing. Tribology International. 2018;120:105-14.
[34] Lemaitre J, Desmorat R. Engineering damage mechanics: ductile, creep, fatigue and brittle failures: Springer Science & Business Media; 2005.
[35] Wang Z, Zhou Q. Applying a population growth model to simulate wear of rough surfaces during running-in. Wear. 2012;294-295:356-63.
[36] Archard J. Contact and rubbing of flat surfaces. Journal of applied physics. 1953;24:981-8.
[37] ISO 25178-2:2012 Surface texture: Areal. Part 2: Terms, definitions and surface texture parameters. Switzerland: BSI; 2012.

[38] Gould B, Greco A. The Influence of Sliding and Contact Severity on the Generation of White Etching Cracks. Tribology Letters. 2015;60.
[39] Gould B, Greco A. Investigating the Process of White Etching Crack Initiation in Bearing Steel. Tribology Letters. 2016;62.
[40] Lubrecht AA, Venner CH, Colin F. Film thickness calculation in elasto-hydrodynamic lubricated line and elliptical contacts: The Dowson, Higginson, Hamrock contribution. Proceedings of the Institution of Mechanical Engineers, Part J: Journal of Engineering Tribology. 2009;223:511-5.
[41] Bower A. The influence of crack face friction and trapped fluid on surface initiated rolling contact fatigue cracks. Journal of Tribology. 1988;110:704-11.
[42] Wei J, Zhang A, Gao P. A study of spur gear pitting under EHL conditions: Theoretical analysis and experiments. Tribology International. 2016;94:146-54.
[43] Rycerz P, Olver A, Kadiric A. Propagation of surface initiated rolling contact fatigue cracks in bearing steel. International Journal of Fatigue. 2017;97:29-38.
[44] Ren N, Zhu D, Wang QJ. Three-Dimensional Plasto-Elastohydrodynamic Lubrication (PEHL) for Surfaces with Irregularities. Journal of Tribology. 2011;133:031502.
[45] Greco A, Sheng S, Keller J, Erdemir A. Material wear and fatigue in wind turbine Systems. Wear. 2013;302:1583-91.